

## 1 **Supplementary Methods**

2

### 3 **Sample acquisition and preparation**

4 Complete shells of *Rastellum diluvianum* and *Acutostrea incurva* oysters and *Biradiolites*  
5 *suecicus* rudists were obtained from the Ivö Klack, Åsen and Maltesholm localities of the  
6 Kristianstad Basin (see **Fig. 1** in main text). These localities in the Kristianstad Basin have been  
7 the subject of several paleoecological and paleoenvironmental studies and are known for their  
8 high species richness and excellent shell preservation (<sup>56</sup>Surlyk and Christensen, 1974; <sup>27</sup>Surlyk  
9 and Sørensen, 2010 <sup>38</sup>Sørensen et al., 2012; <sup>45</sup>2015; <sup>26</sup>de Winter et al., 2020). Given a maximum  
10 burial depth of 40 meters (<sup>27</sup>Surlyk and Sørensen, 2010) and a geothermal gradient of at most  
11 30°C/km<sup>57</sup>, the sediments and fossils of the Kristianstad Basin localities did not exceed the  
12 temperature threshold (80°C) required to allow solid state reordering to take place (<sup>43</sup>Fernandez  
13 et al., 2020; <sup>44</sup>Henkes et al., 2014). We can therefore safely assume that this process did not  
14 affect the clumped isotope signature of the specimens in this study. Specimens of *R. diluvianum*  
15 were found *in situ* attached to the vertical sides of large boulders that characterized the rocky  
16 shore of Ivö Klack, while *A. incurva* and *B. suecicus* were found in life position associated with  
17 deeper (5-15m) paleoenvironmental settings below fair weather wave base and surrounded by  
18 fragments from other shelly fauna (<sup>56</sup>Surlyk and Christensen, 1974). All localities were  
19 biostratigraphically assigned to the latest early Campanian *B. mammillatus* belemnite zone and  
20 re-dated to 78.14 ± 0.26 Ma using *in situ* specimen by specimen strontium isotope stratigraphy  
21 dating (see <sup>26</sup>de Winter et al., 2020).

22 Shells from *A. incurva* and *B. suecicus* were subject to chemical investigation in <sup>45</sup>Sørensen et al.  
23 (2015), for which they were prepared as thick sections mounted on glass slides with polished  
24 cross sections through the axis of maximum growth exposed for chemical analyses (see  
25 <sup>45</sup>Sørensen et al., 2015). Valves of *R. diluvianum* were cleaned and fully embedded in Araldite®  
26 2020 epoxy resin (Bodo Möller Chemie Benelux, Antwerp, Belgium). Dorsoventral slabs ( $\pm 10$   
27 mm thick) were cut perpendicular to the hinge line using a water-cooled slow rotating saw with a  
28 diamond-coated blade (blade thickness  $\pm 1$  mm; Fig. 2). The surfaces cut on the central growth  
29 axis were progressively polished using silicon-carbide polishing disks (up to P2500, or 8.4  $\mu\text{m}$   
30 grain size).

31

## 32 **Preservation**

33 In order to assess shell preservation, polished surfaces of all shells were scanned at high (6400  
34 dpi, pixel size of 4  $\mu\text{m}^2$ ) resolution using an Epson Perfection 1650 flatbed color scanner (Seiko  
35 Epson Corp., Suwa, Japan). Shell microstructures were studied in detail on high-resolution scans  
36 and by using reflected light optical microscopy. Microstructural features were used to reconstruct  
37 the relative timing of shell growth (see <sup>45</sup>Sørensen et al., 2015 for *A. incurva* and *B. suecicus* and  
38 <sup>26</sup>de Winter et al., 2020 and **Fig S1** for *R. diluvianum*). Fragments of visually well-preserved  
39 material from different microstructures in the shells were coated with gold and studied under a  
40 Scanning Electron Microscope (Quanta 200 ESEM) and imaged at 1000x–2000x magnification  
41 to study the preservation of original calcite microstructures at the microscopic level (see **Fig. S1**  
42 and <sup>26</sup>de Winter et al., 2020). Full size micrographs and SEM images used for assessing  
43 preservation of shell structure at the microscopic level are freely accessible in the online  
44 supplement of <sup>26</sup>de Winter et al., 2020 (<https://doi.org/10.5281/zenodo.2581304>).

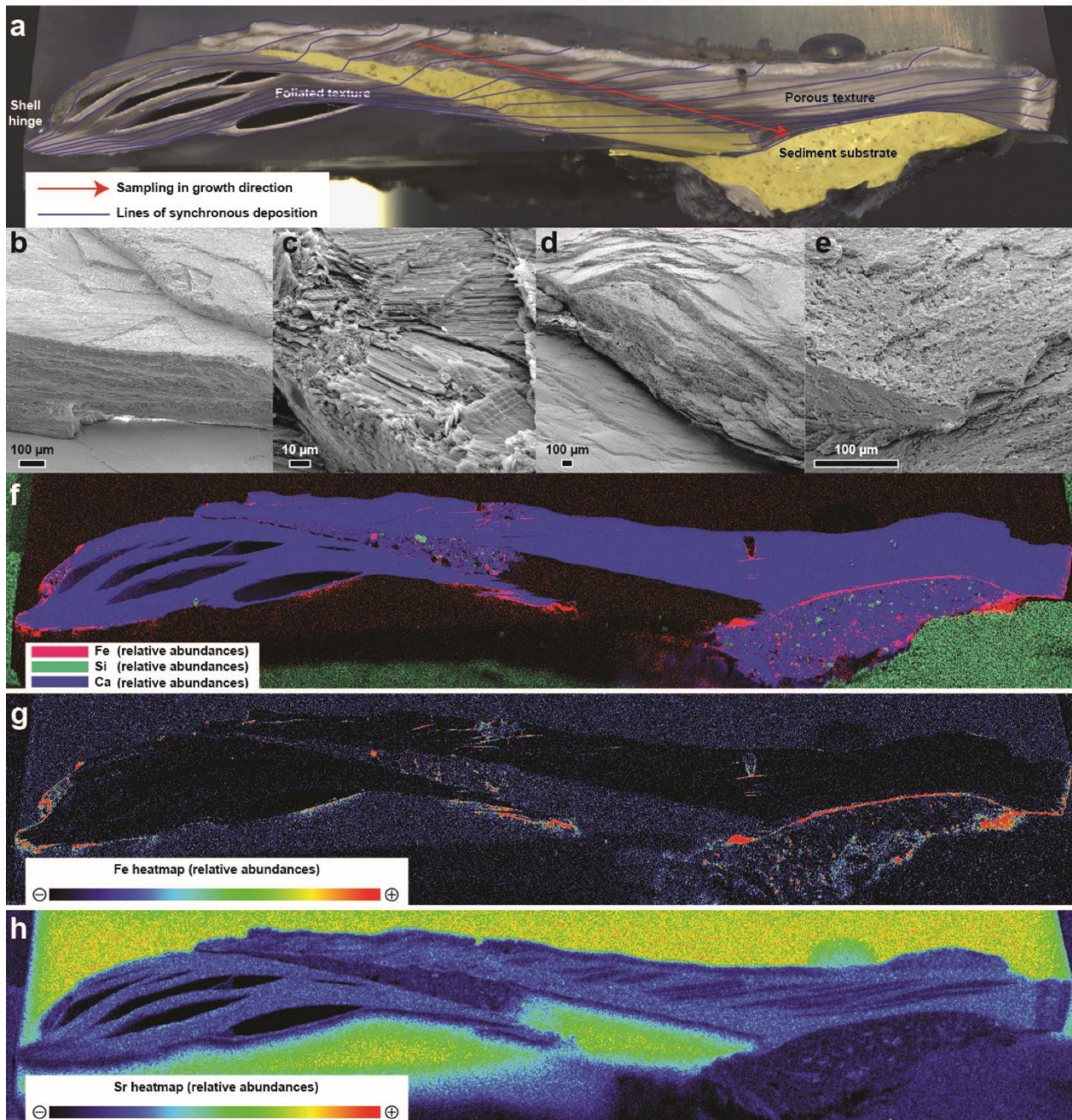
45 Elemental abundance maps of all shell cross sections were obtained using a Bruker Tornado M4  
46 energy-dispersive micro-X-Ray Fluorescence scanner ( $\mu$ XRF; Bruker nano GmbH, Berlin,  
47 Germany). The  $\mu$ XRF is equipped with a Rh metal-ceramic tube X-Ray source filament operated  
48 at 50 kV and 600  $\mu$ A (30 W; maximum energy settings). The circular spot projected on the  
49 sample surface is calibrated to have a diameter of 25  $\mu$ m (Mo-K $\alpha$ ). A  $\mu$ m-precision XYZ  
50 translation stage allows for quick and precise sample movement such that a grid of 25  $\mu$ m XRF  
51 spots can be measured on the sample surface by continuous scanning to construct elemental  
52 maps. Exposure times of the X-ray beam per sampling position in mapping mode (1 ms/pixel)  
53 are too short to gain adequate signal-to-noise ratio for pixel-by-pixel quantification of elemental  
54 concentrations. Instead, processing of entire map surfaces using the Bruker Esprit™ software  
55 allows semi-quantitative elemental abundance maps to be created of the sample surface based on  
56 a mapping of the count rate in ‘Regions of Interest’ of elements (see <sup>58</sup>de Winter and Claeys,  
57 2016; <sup>39</sup>de Winter et al., 2017; **Fig S1**). XRF maps allow for a rapid assessment of the  
58 preservation state of original shell calcite based on variations in Si, Mn, Fe and Sr concentrations  
59 (<sup>58</sup>de Winter and Claeys, 2016; **Fig. S1**). An example of  $\mu$ XRF map result on *R. diluvianum* is  
60 given in **Fig. S1**, others are provided in <sup>26</sup>de Winter et al. (2020) and freely accessible in its  
61 online supplement (<https://doi.org/10.5281/zenodo.2581304>).

62 Quantitative  $\mu$ XRF line scans were measured in growth direction on shell cross sections to  
63 obtain profiles of trace elements serving as indicators of diagenesis. Line scans were carried out  
64 in point-by-point analysis mode (e.g. <sup>59</sup>de Winter et al., 2017). Dwell times of 60 seconds per  
65 measurement point yielded sufficiently high signal-to-noise ratios for individual points in line  
66 scans to be quantified. This acquisition time was chosen so as to provide the optimal compromise  
67 between increasing run time (improved signal/noise ratio; enhanced reproducibility) and

68 increasing the number of sampling positions (improving sampling density and allowing duplicate  
69 measurements) for the elements Mg, Al, Si, P, S, Ca, Ti, Mn, Fe, Cu, Zn and Sr (see discussion  
70 in <sup>39</sup>de Winter et al., 2017). The sampling interval of line scans was 50 µm, allowing detailed  
71 investigation of local diagenetic features within the visually well-preserved foliated calcite.  
72 Spectra were quantified using the Bruker Esprit software calibrated using the matrix-matched  
73 BAS-CRM393 limestone standard (Bureau of Analyzed samples, Middlesbrough, UK), after  
74 which individual measurements were calibrated offline using 7 matrix-matched certified  
75 reference materials (CCH1, COQ1, CRM393, CRM512, CRM513, ECRM782 and SRM1d),  
76 which were treated as samples (see <sup>60</sup>Vansteenberge et al., 2020). R<sup>2</sup> values of calibration curves  
77 exceeded 0.99 and reproducibility standard deviations were better than 10% relative to the mean.  
78 A preservation check was carried out on all specimens and areas of the shell were rejected based  
79 on conservative thresholds for diagenetic recrystallization or detrital contamination ([Ca] < 38  
80 wt%, [Si] > 1 wt%, [Mn] > 200 µg/g or [Fe] > 250 µg/g; [Sr]/[Mn] < 100 mol/mol; see <sup>61</sup>Al-  
81 Aasm and Veizer, 1986; <sup>45</sup>Sørensen et al., 2015). Plots and raw results of XRF linescans used for  
82 assessing preservation of shell structure at the microscopic level are freely accessible in the  
83 online supplement of <sup>26</sup>de Winter et al., 2020 (<https://doi.org/10.5281/zenodo.2581304>).  
84 Based on these analyses, the best-preserved specimen was selected for each species (*Rastellum*  
85 *diluvianum*, *Acutostrea incurva* and *Biradiolites suecicus*) to sample for clumped isotope  
86 analyses. The stable oxygen isotope results (δ<sup>18</sup>O<sub>c</sub>) for these specimens as reported in the  
87 previous studies by <sup>45</sup>Sørensen et al. (2015) and <sup>26</sup>de Winter et al. (2020) were used to augment  
88 the sample size for δ<sup>18</sup>O<sub>sw</sub> reconstructions in this study. Full methodologies for mass  
89 spectrometry used to obtain these δ<sup>18</sup>O<sub>c</sub> measurements are found in the respective publications.  
90 The full methodology for new δ<sup>18</sup>O<sub>c</sub> and Δ<sub>47</sub> stable isotope analyses carried out in this study is

91 detailed below. A posteriori assessment of preservation based on stable isotope results from this  
92 and previous studies (<sup>45</sup>Sørensen et al., 2015 and <sup>26</sup>de Winter et al. 2020) was carried out by  
93 comparing results with isotopic features of local diagenetic carbonate fabrics in Kristianstad  
94 Basin, which were characterized by a  $\delta^{18}\text{O}_c$  value of around -0.5‰ (see discussion in <sup>45</sup>Sørensen  
95 et al., 2015 and <sup>26</sup>de Winter et al. 2020). Outliers in stable isotope data in the direction of these  
96 diagenetic signatures (see highliers in panels A-C and F of **Fig. S3**) were not considered for  
97 temperature and  $\delta^{18}\text{O}_{sw}$  reconstructions.

## Preservation of *R. diluvianum*



98

99 **Fig S1:** Image highlighting good preservation of *R. diluvianum* and an example of the combined  
100 microscopy and  $\mu\text{XRF}$  approach for preservation assessment. Figure was adapted with slight  
101 modifications from de Winter et al., 2020. Panel (a) contains a high-resolution color scan of the  
102 cross section through *R. diluvianum* on which the different shell textures as well as the directions

103 *of high-resolution analyses (in growth direction) are indicated. Areas marked in yellow*  
104 *represent sediment infilling below and within the valves. (b) and (c) show SEM images of the*  
105 *well-preserved foliated calcite in the shell. More porous structures in the shell (chalky calcite)*  
106 *are depicted in SEM images shown in (d) and (e). These porous structures were avoided during*  
107 *sampling and only the well-preserved foliated calcite was sampled. Below are shown three XRF*  
108 *elemental maps of the same cross section: An RGB-colored map displaying the relative*  
109 *abundances of Fe, Si and Ca (f), A heatmap of Fe concentrations (g; see scalebar below map)*  
110 *and a heatmap of Sr concentrations (h; see scalebar below map). XRF mapping only yields*  
111 *relative (semi-quantitative) abundance of elements.*

112

### 113 **Seasonality reconstructions based on stable isotope records from skeletal hardparts**

114 The presence of clear periodicity in  $\delta^{18}\text{O}_c$  records and consistent phase relationships between  
115 different geochemical proxies (<sup>62</sup>Ivany, 2012; <sup>26</sup>de Winter et al., 2020) suggests that this cyclicity  
116 governs changes in calcification rate or strong environmental forcing. Similar periodic behavior  
117 observed in geochemical proxy records measured in a wide range of modern and fossil bivalves  
118 (e.g. <sup>63</sup>Jones, 1983; <sup>64</sup>Goodwin et al., 2001; <sup>65</sup>Schöne et al., 2005; <sup>10</sup>Steuber et al., 2005;  
119 <sup>66</sup>Batenburg et al., 2011). The preservation of seasonal variation in stable isotope ratios ( $\delta^{13}\text{C}$  and  
120  $\delta^{18}\text{O}_c$ ) has been demonstrated in a wide range of bivalve species, and the periodicity found in this  
121 study's specimens strongly resembles these seasonal cycles (e.g. <sup>67</sup>Steuber, 1996; <sup>68</sup>Surge et al.,  
122 2001; <sup>65</sup>Schöne et al., 2005; <sup>69</sup>Elliot et al., 2008). In addition, similar seasonal cyclicity in Mg/Ca  
123 and Sr/Ca ratios in modern and fossil bivalve shells has been described in previous studies  
124 (<sup>70</sup>Steuber, 1999; <sup>71</sup>Freitas et al., 2006; <sup>72</sup>Surge and Lohmann, 2008; <sup>73</sup>Ullmann et al., 2013;

125 <sup>74</sup>Mouchi et al., 2013). The relationship between  $\delta^{18}\text{O}_c$  and calcification temperature and salinity  
126 often results in seasonal changes in these parameters to be strongly expressed in bivalve shell  
127 records (<sup>68</sup>Surge et al., 2001). In a multi-proxy sclerochronology study, the seasonality in  $\delta^{18}\text{O}_c$   
128 can therefore be used to demonstrate seasonal cyclicality in other proxy records. In fossil bivalve  
129 shells, confidence can be obtained from the fact that the seasonal cycle is one of the strongest  
130 sources of periodic variation in the marine environment (<sup>75</sup>Mitchell, 1976; <sup>76</sup>Huybers and Curry,  
131 2006). To fit periodicity on the scale of millimeters to centimeters to other environmental cycles  
132 (e.g. diurnal or tidal cyclicality) would require extremely fast growth rates (> 40 cm/yr) which are  
133 not observed in modern bivalves. Natural periods of environmental variability longer than a year  
134 but shorter than the lifespan of the longest-living known bivalve species (*Arctica islandica*,  $\pm 500$   
135 yr) are known to affect shell calcification but cannot explain the consistency and high amplitude  
136 of variability observed in seasonal cycles (<sup>65</sup>Schöne et al., 2005).

137 One problem with the interpretation of sclerochronology records is the lack of independent  
138 control on the ontogenetic age of fossil bivalve shells. No absolute method exist that allows  
139 dating of fossil bivalves with a precision better than a year. Therefore, it is not possible to  
140 independently verify the ontogenetic age of a fossil shell, and interpretation of seasonality in  
141 these records must rely on comparison with modern analogues with known ontogenetic ages.  
142 This (so far) also prevents the creation of so-called “master curves” made from the records of  
143 multiple shells that grew simultaneously (<sup>77</sup>Butler et al., 2010) in deep time settings. Intra-shell  
144 comparisons in such master curves allow an assessment of the reproducibility of seasonal  
145 cyclicality in proxy records between the shells of contemporaneous bivalves and the creation of  
146 long continuous seasonally resolved sclerochronology records (<sup>78</sup>Marali et al., 2017). Results  
147 from modern intra-shell comparisons grown in the same year show that seasonality in stable

148 isotope and trace element proxies is reproducible between bivalves of the same species and  
149 environment (<sup>78</sup>Marali et al., 2017). Based on these considerations and on the discussion in <sup>26</sup>de  
150 Winter et al. (2020) we conclude that variability observed in  $\delta^{18}\text{O}_c$  records in this study can only  
151 be seasonal in origin.

152 Although winter growth stops are more common in modern bivalves (e.g. <sup>33</sup>Lartaud et al., 2010),  
153 summer stops are known from modern oysters (<sup>79</sup>Kirby et al., 1998; <sup>68</sup>Surge et al., 2001) and  
154 from fossil bivalves from greenhouse periods (<sup>80</sup>Buick and Ivany, 2004; <sup>39</sup>de Winter et al., 2017).  
155 Sparsely available data suggests that in greenhouse climates summer stops may be more  
156 common, even in high-latitude settings (<sup>80</sup>Buick and Ivany, 2004). The fact that  $\delta^{18}\text{O}_c$  records  
157 from specimens in this study contain datapoints in all monthly time bins shows that, while  
158 growth definitely slowed down in the studied specimens (as is evident from uneven  
159 representation of various months), growth cessations over periods of more than one month, or  
160 consistent growth stops in the same month throughout ontogeny are highly unlikely.

161

## 162 **Age model**

163 In order to establish chronologies for geochemical proxy records through the life span of bivalve  
164 species, age models need to be constructed for each individual shell. In modern bivalves,  
165 microgrowth patterns often enable the creation of shell chronologies independent from the  
166 geochemical records, because in many species of bivalve microgrowth features (e.g. growth  
167 increments or growth lines) can be linked to periodicity in the animal's environment (e.g.  
168 <sup>63</sup>Jones, 1983; <sup>81</sup>Dauphin et al., 1989; <sup>65</sup>Schöne et al., 2005; <sup>62</sup>Ivany 2012). Alternatively, modern  
169 bivalves are often labeled with calcein or elevated trace element concentrations (e.g. <sup>82</sup>Schöne et

170 al. 2005; <sup>83</sup>Barbin et al., 2008; <sup>74</sup>Mouchi et al., 2013; <sup>84</sup>Ballesta-Artero et al., 2018). However, in  
171 deep time fossil specimens, such as those used in this study, these techniques are not available,  
172 and microgrowth structures of fossil species only distantly related to modern relatives (e.g. the  
173 rudist *B. suecicus*) are often difficult to interpret, if they are deposited (and preserved) at all.  
174 Furthermore, oysters (like *A. incurva* and *R. diluvianum*) are notoriously lacking reliable  
175 indicators of growth periodicity in their shell structures (<sup>29</sup>Huyghe et al., 2019), making  
176 independent chronologies unavailable for shells used in this study.

177 An alternative solution for establishing shell chronology is to base these chronologies on the  
178 seasonal patterns observed in geochemical records, such as those of  $\delta^{18}\text{O}_c$  (<sup>85</sup>Goodwin et al.,  
179 2003; <sup>50</sup>Judd et al., 2018), Mg/Ca (<sup>86</sup>Durham et al., 2017) or  $\delta^{13}\text{C}$  (<sup>87</sup>de Winter et al., 2020). Over  
180 the past years, multiple attempts have been made to create statistical routines for interpolating  
181 growth timing from seasonally fluctuating patterns in these proxies, which is not straightforward  
182 due to the complexity of simultaneous and out of phase changes in growth rate and multiple  
183 factors in the animal's environment (<sup>88</sup>Wilkinson and Ivany, 2002; <sup>89</sup>Goodwin et al., 2009;  
184 <sup>50</sup>Judd et al., 2018). In this study, we apply the most sophisticated model for linking  $\delta^{18}\text{O}_c$  to  
185 shell chronology to date (<sup>50</sup>Judd et al., 2018). This model simulates the  $\delta^{18}\text{O}_c$  curve by combining  
186 sinusoid curves for both growth rate and temperature and using a  $\delta^{18}\text{O}_c$ -temperature equation  
187 assuming the shell is precipitated in equilibrium with the sea water (as shallow marine bivalves  
188 are commonly assumed to do). According to <sup>50</sup>Judd et al., 2018, this combination of two sinusoid  
189 curves accurately approximates seasonal patterns in  $\delta^{18}\text{O}_c$  recorded in a range of modern bivalve  
190 shells from the literature. In this procedure, growth rate variability (simulated as a skewed  
191 sinusoid curve) is used to link the modeled seasonal temperature sinusoid to distance along the  
192 record. This temperature record is then converted to a  $\delta^{18}\text{O}_c$  record, assuming a constant  $\delta^{18}\text{O}_{\text{sw}}$

193 composition. The resulting simulated  $\delta^{18}\text{O}_c$  record is compared to the measured  $\delta^{18}\text{O}_c$  record.  
194 The original version of the model was written for aragonitic shells but was adapted for calcite  
195 species using the Kim and O'Neil (<sup>17</sup>1997)  $\delta^{18}\text{O}_c$ -temperature relationship (see <sup>26</sup>de Winter et al.,  
196 2020). While this model is based on the shape of seasonal  $\delta^{18}\text{O}_c$  oscillations, a detailed  
197 examination of the relative influence of SST and  $\delta^{18}\text{O}_{sw}$  variability on these curves in a wide  
198 range of modern settings demonstrates that changes in the shape of the  $\delta^{18}\text{O}_c$  curve due to the  
199 influence of  $\delta^{18}\text{O}_{sw}$  variability do not compromise the accuracy of the modelled shell ages<sup>20</sup>.  
200 Since monthly time binning for seasonality reconstructions in this study is independent of the  
201 phase of the  $\delta^{18}\text{O}_c$  seasonality, age modelling will be sufficiently accurate as long as annual  
202  $\delta^{18}\text{O}_c$  oscillations can be resolved in the shell (regardless of their phase and amplitude), which is  
203 the case for all three specimens. These properties of the age model allow alignment of shell  
204 records based on  $\delta^{18}\text{O}_c$  oscillations without making the resulting seasonality reconstructions  
205 dependent on  $\delta^{18}\text{O}_c$ , which would compromise the independence of the new clumped isotope  
206 seasonality method. The adapted MATLAB script used for age model construction is found in  
207 **Supplementary Data 9** and the raw results of the model are provided in **Supplementary Data**  
208 **1**.

209

## 210 **Clumped isotope analyses**

211 Clumped isotope ( $\Delta_{47}$ ) analyses were carried out on Thermo Fisher Scientific MAT253 and 253  
212 PLUS mass spectrometers coupled to a Kiel IV carbonate preparation device. Calcite samples  
213 (individual replicates of  $\sim 90$   $\mu\text{g}$  for 253Plus and  $\sim 150$   $\mu\text{g}$  for MAT253) were reacted at  $70$   $^\circ\text{C}$   
214 with nominally anhydrous (103%) phosphoric acid. The resulting  $\text{CO}_2$  gas was cleaned from  
215 water and organic compounds with two cryogenic LN2 traps and a PoraPak Q trap kept at  $-40$

216 °C. The purified sample gases were analyzed in micro-volume LIDI mode with 400 s integration  
217 time against a clean CO<sub>2</sub> working gas ( $\delta^{13}\text{C} = -2.82\text{‰VPDB}$ ;  $\delta^{18}\text{O} = -4.67\text{‰VPDB}$ ;  $\Delta_{47} = 0\text{‰}$ ),  
218 corrected for the pressure baseline (<sup>47</sup>Bernasconi et al., 2013; <sup>48</sup>Meckler et al., 2014) and  
219 converted into the absolute reference frame by creating an empirical transfer function from the  
220 daily analyzed ETH calcite standards (ETH-1, -2, -3) and their accepted values (<sup>47</sup>Bernasconi et  
221 al., 2018). All isotope data were calculated using the new IUPAC parameters following <sup>49</sup>Daëron  
222 et al. (2016) and  $\Delta_{47}$  values were projected to a 25 °C acid reaction temperature with a correction  
223 factor of 0.071 ‰ (after <sup>22</sup>Petersen et al., 2019). Long-term  $\Delta_{47}$  reproducibility standard  
224 deviation was 0.04‰ (0.039‰ for MAT253 Plus and 0.045‰ for MAT253) based on repeated  
225 measurements of ~100 µg aliquots of our check standard IAEA C2 ( $\Delta_{47}$  of 0.719‰; measured  
226 over a 20-month period; see **Supplementary Data 8** for details). No statistical difference was  
227 found between results from both instruments (see **Supplementary Data 8**). For the  $\delta^{18}\text{O}_c$   
228 compositions we applied an acid correction factor of 1.00871 (<sup>17</sup>Kim and O’Neil, 1997) and  
229 reported versus VPDB with a reproducibility of 0.13‰ (95% confidence level). Results were  
230 combined with  $\delta^{18}\text{O}_c$  data previously measured in the same shells (<sup>45</sup>Sørensen et al., 2015; <sup>26</sup>de  
231 Winter et al., 2020; see **Supplementary Data 2**) to improve the confidence of seasonal age  
232 models and the temporal resolution of SST and  $\delta^{18}\text{O}_{\text{sw}}$  reconstructions.

233

### 234 **Statistical evaluation of incrementally sampled $\Delta_{47}$ aliquots for reconstructing absolute sea** 235 **surface temperature seasonality**

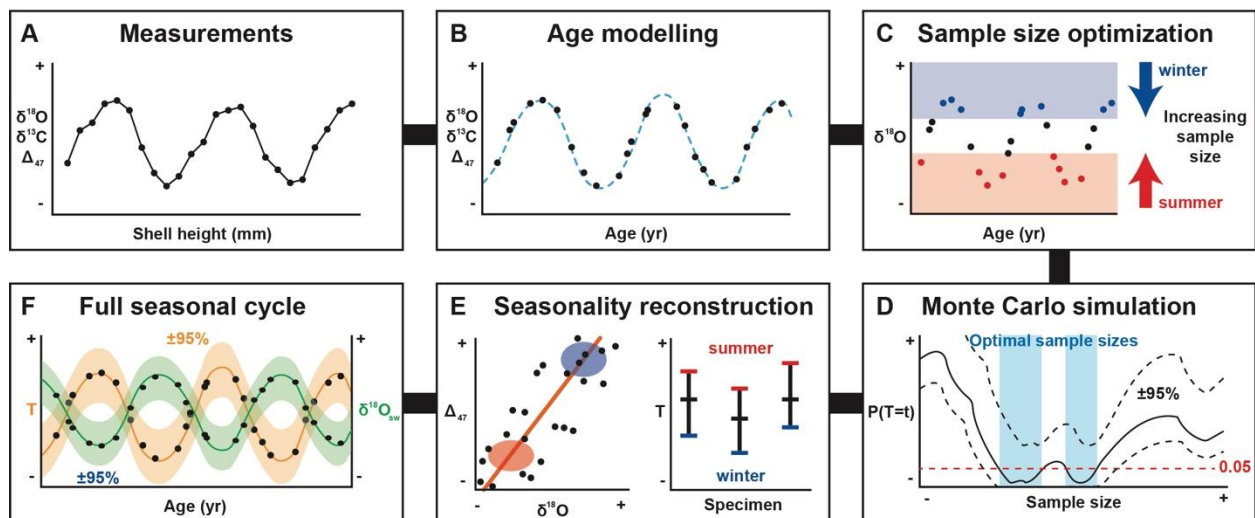
236 The relatively high uncertainty on  $\Delta_{47}$  measurements of individual 100 µg aliquots translate  
237 to a standard deviation of ~10°C (see **Supplementary Data 8**) on individual aliquots.  
238 Reconstructing absolute temperature seasonality from incrementally sampled small aliquot

239 clumped isotope analyses therefore requires combining samples from seasons or months.  
240 Reproducibility tests on homogenous samples show that precise  $\Delta_{47}$  measurements ( $2\sigma$  of  
241 0.013‰, or 3-4°C) typically require a minimum of 14 replicates of 90-120  $\mu\text{g}$  (1-2 mg;  
242 <sup>25</sup>Fernandez et al., 2017; <sup>47</sup>Bernasconi et al., 2018). In fast-growing bio-archives (e.g. *Porites*  
243 corals: ~10 mm/yr; <sup>90</sup>Lough and Barnes, 2000; coralline algae: ~5 mm/yr; <sup>91</sup>Adey and Vassar,  
244 1975 and mollusks: <20 mm/yr; <sup>85</sup>Goodwin et al., 2003; <sup>92</sup>Gentry et al., 2008; this study) such a  
245 sample size would require very high resolution sampling (>30 samples/year) to resolve seasonal  
246 variability. Previous studies on pelagic marine foraminifer records have applied sliding window  
247 Monte Carlo simulations to capture high-resolution (kyr-scale) variability in SST and  $\delta^{18}\text{O}_{\text{sw}}$   
248 (<sup>93</sup>Rodríguez-Sanz et al., 2017). Due to limitations on sampling resolution (>100  $\mu\text{m}$ ), such a  
249 moving window approach would severely dampen the recovered seasonal cycle in typical  
250 seasonality archives (see discussion in <sup>20</sup>). Larger samples of aliquots technically result in  
251 reduced uncertainties on the temperature estimates but smooth out more seasonal variability,  
252 while smaller sample sizes allow more extreme seasons to be captured at the cost of instrumental  
253 reproducibility. Therefore, a routine was developed to find the optimal sample size for  
254 combining aliquots from summer and winter seasons while compromising between these two  
255 effects. A step-by-step explanation of this routine as well as a detailed evaluation of its precision  
256 and accuracy on a range of  $\Delta_{47}$ -  $\delta^{18}\text{O}_{\text{c}}$  datasets is provided in <sup>20</sup>. For the purpose of this study, the  
257 routine is illustrated in detail below. Absolute SST seasonality was reconstructed from  $\Delta_{47}$  data  
258 in six steps (see **Fig. S2** and **S3**):

- 259 1.  $\delta^{18}\text{O}_{\text{c}}$  and  $\Delta_{47}$  data are aligned relative to the annual cycle using an age modelling routine  
260 developed by Judd et al. (<sup>50</sup> see **Fig. S2A-B** and explanation above)

- 261 2. Multiple aliquots were combined to reduce the uncertainty on monthly temperature  
 262 estimates (**Fig. S2C**)
- 263 3. The optimum sample size was found as that which achieved the most statistically  
 264 significant ( $p \leq 0.05$ ) separation between summer and winter  $\Delta_{47}$  averages using a sliding  
 265 window Student's T-test (**Fig. S2D**).
- 266 4. Uncertainties on  $\delta^{18}\text{O}_c$  and  $\Delta_{47}$  analyses were propagated through this optimization  
 267 procedure using Monte Carlo simulations (**Fig. S2D**).
- 268 5. Summer and winter SST and  $\delta^{18}\text{O}_{\text{sw}}$  and their uncertainties were reconstructed from  
 269 optimal samples of multiple aliquots (**Fig. S2E**).
- 270 6. The relationship between  $\Delta_{47}$  and  $\delta^{18}\text{O}_c$  in these reconstructions and the  $\delta^{18}\text{O}_c$  record  
 271 were used to reconstruct sub-annual SST and  $\delta^{18}\text{O}_{\text{sw}}$  by binning  $\Delta_{47}$  and  $\delta^{18}\text{O}_c$  data into  
 272 monthly time bins (**Fig. S2F**). Seasonality was defined based on average temperature  
 273 estimates of the warmest and coldest month.

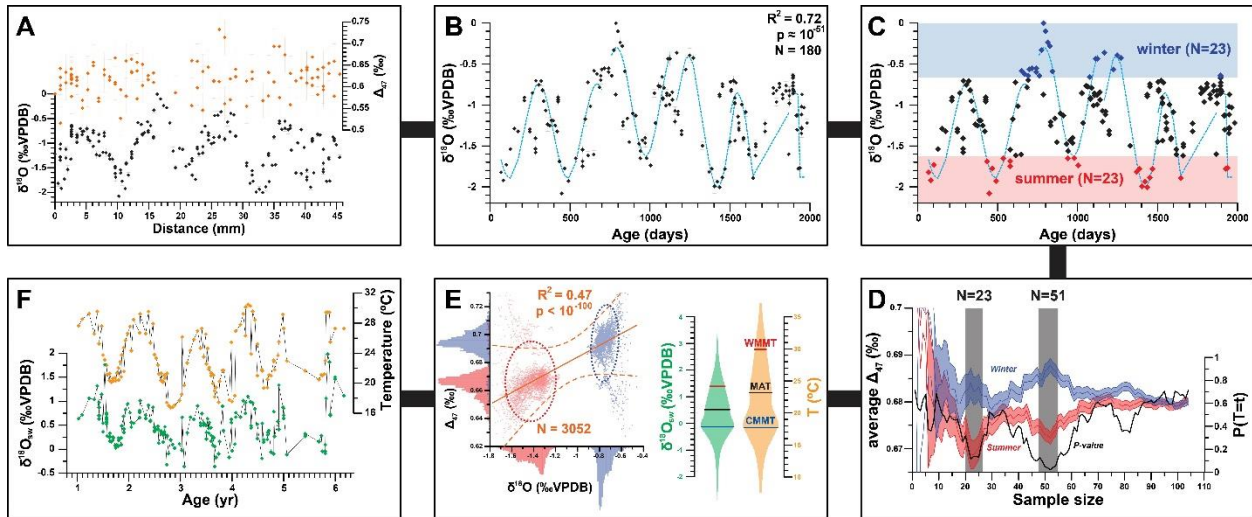
### Workflow for clumped isotope seasonality reconstructions



274 **Fig. S2:** Illustration of the workflow employed to reconstruct absolute SST and  $\delta^{18}\text{O}_{\text{sw}}$   
 275 seasonality from  $\delta^{18}\text{O}_c$  and  $\Delta_{47}$  measurements (A) aligned to an age model (B). Sample sizes are  
 276

277 optimized for winter and summer reconstructions (C-D). Monte Carlo simulations of this  
 278 optimization are applied to the  $\delta^{18}O_c$  data to obtain sub-seasonally resolved SST and  $\delta^{18}O_{sw}$   
 279 results (E-F). See text for details.

280



281

282 **Fig. S3:** Results of applying the optimization and modelling workflow in Fig. S2 on  
 283 measurements from *R. diluvianum*. Details in text. Shaded envelopes in D and ellipses in E  
 284 represent 95% confidence intervals.

285

286 **Optimal sample size calculations**

287 Sample groups of  $\Delta_{47}$  values and associated  $\delta^{18}O_c$  values in aliquots are created by including  
 288 increasing amounts of aliquots from both the low end (summers) and the high end (winters) of  
 289 the  $\delta^{18}O_c$ -range. For each sample size (number of aliquots), temperatures and seawater oxygen  
 290 isotope compositions and their uncertainties are calculated for both the light oxygen isotope  
 291 (summer) and heavy oxygen isotope (winter) group. Note also that all summers and winters

292 recorded in the entire shell transect are used in these calculations and that reconstructed  
293 temperatures reflect average summers and winter temperatures in the record. The success of each  
294 chosen sample size is evaluated by calculating the p-value of the difference between the summer  
295 and winter temperatures and their uncertainties by means of a Student's T-test ( $P(T < t)$ ). The  
296 lowest p-values determine the optimum sample size and the ideal compromise between low  
297 temperature uncertainty and extreme seasonality reconstruction. After the summer and winter  
298 endmembers for the record are established, all  $\Delta_{47}$  and  $\delta^{18}\text{O}_c$  data are ordered relative to these  
299 endmembers and the age model and grouped into monthly time bins.

300

### 301 **Monte Carlo simulations**

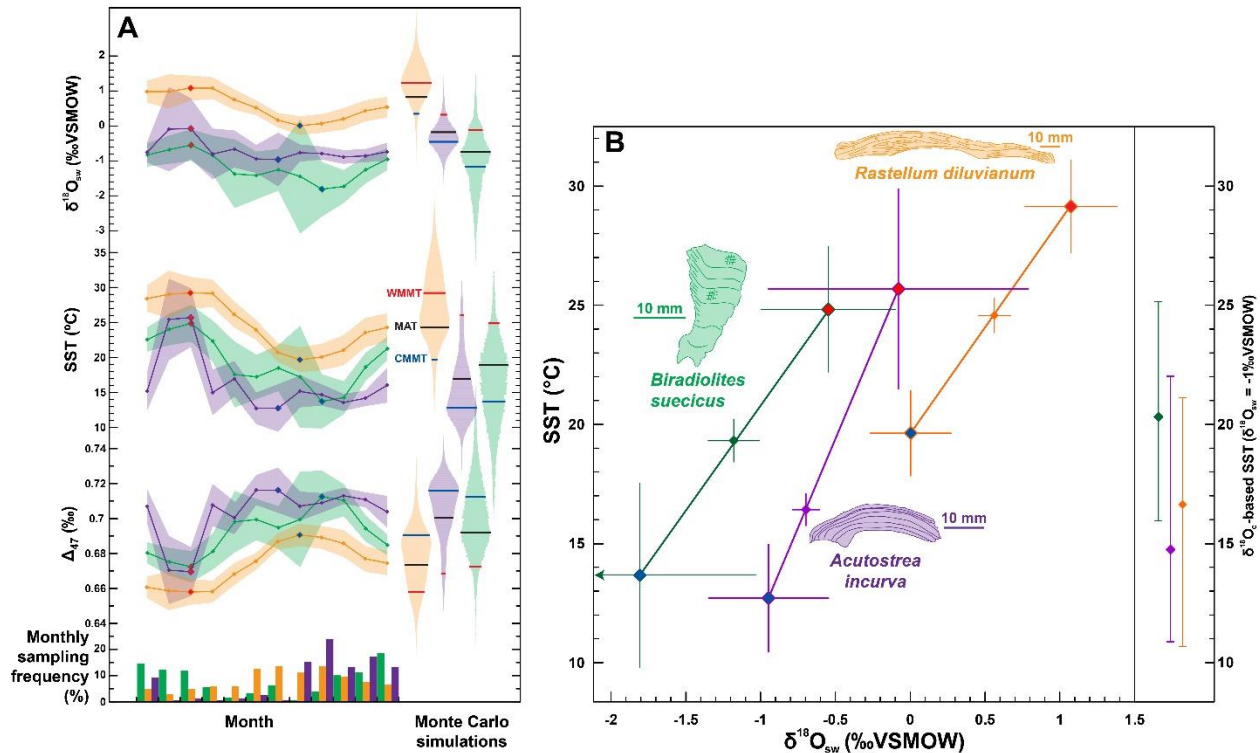
302 In order to allow uncertainties on individual  $\Delta_{47}$  and  $\delta^{18}\text{O}_c$  measurement to be taken into account  
303 in this assessment of optimal sample size and extreme temperature seasonality, the routine  
304 described above was repeated 1000 times on  $\Delta_{47}$  and  $\delta^{18}\text{O}_c$  records randomly sampled based on  
305 their measured value and measurement uncertainty in a Monte Carlo simulation approach. The  
306 distribution of uncertainty around the measured value is assumed to be normal. Sampling from  
307 these error distributions produced 1000 different sets of  $\Delta_{47}$  and  $\delta^{18}\text{O}_c$  records, which were  
308 subject to the optimal sample size calculations outlined above. Of all sample sizes of 1000  
309 simulations of moving-window p-tests, only those simulations with statistically significant  
310 separation between summer and winter temperatures ( $p < 0.05$ ) were used. The distribution of  
311 sample sizes among these successful simulations as well as an overview of the distribution of p-  
312 values of all simulated sample groups is given in **Supplementary Data 3**. The distribution of  
313 statistically significant sample sizes for the *Rastellum diluvianum* shell exhibits peaks at sizes of  
314 21 and 50 aliquots, showing that summer and winter temperatures can be best distinguished

315 using these sample sizes (see **Fig. S3**). The temperatures and  $\delta^{18}\text{O}_{\text{sw}}$  values reconstructed from  
316 all successful grouping of summer and winter aliquots are reported in **Supplementary Data 3**.

317

### 318 **Calculating seasonality**

319 Since the optimal sample size for summer and winter temperature reconstructions are relatively  
320 large (>20 aliquots), this method reconstructs a somewhat dampened temperature seasonality.  
321 However, using the results of the Monte Carlo simulation outlined above, it is possible to back-  
322 model extreme temperature and  $\delta^{18}\text{O}_{\text{sw}}$  seasonality. This was done by using the relationship  
323 between  $\Delta_{47}$  and the  $\delta^{18}\text{O}_{\text{c}}$  of calcite and applying it on the original  $\delta^{18}\text{O}_{\text{c}}$  record to project  $\Delta_{47}$ ,  
324 and therefore temperature, on each individual aliquot. The slope and intercept described by  $\Delta_{47}$   
325 and  $\delta^{18}\text{O}_{\text{c}}$  reconstructions of summer and winter is therefore calculated in all simulations with  
326 significant p-values. For all these successful simulations, the linear relationship between  $\Delta_{47}$  and  
327  $\delta^{18}\text{O}_{\text{c}}$  described by the summer and winter reconstructions is applied on the full  $\delta^{18}\text{O}_{\text{c}}$  record to  
328 create a large set of individual high-resolution temperature records, from which monthly SST  
329 and  $\delta^{18}\text{O}_{\text{sw}}$  data and 95% confidence envelopes on these reconstructions were constructed. A  
330 summary of the results of this routine is given in **Supplementary Data 3** and the full data of  
331 every propagated Monte Carlo simulation is provided in **Supplementary Data 11**. The result of  
332 these monthly reconstructions and the distribution of  $\Delta_{47}$ , SST and  $\delta^{18}\text{O}_{\text{sw}}$  results obtained  
333 through MC simulations are shown in **Fig. S4**. The full script used to calculate seasonality from  
334 high-resolution clumped isotope data is provided in **Supplementary Data 10**.



335

336 **Fig. S4: Paleoseasonality reconstructions** A) From bottom to top: relative monthly sampling  
 337 frequencies (bar chart), monthly average  $\Delta_{47}$  measurements and monthly SST and  $\delta^{18}O_{sw}$   
 338 reconstructions from *R. diluvianum* (orange), *A. incurva* (purple) and *B. suecicus* (green).  
 339 Shaded envelopes indicate 95% confidence levels and violin plots to the right show the  
 340 distribution of Monte Carlo simulation results. Monthly records are aligned by warmest month  
 341 (red dots), while coldest months are indicated in blue. B) SST and  $\delta^{18}O_{sw}$  reconstructions of  
 342 warmest month (red symbols), coldest month (blue symbols) and annual average (symbols in  
 343 color of specimen). Thin crosses indicate 95% confidence level uncertainties on these estimates.  
 344 To the right, vertical bars indicate summer, winter and MAT estimates one would obtain from  
 345  $\delta^{18}O_c$  while assuming a constant  $\delta^{18}O_{sw}$  of -1‰VSMOW. Drawings represent scaled cross  
 346 sections through the three specimens, with horizontal scale bars indicating 10 mm

347

### 348 **Example results of optimum sample size calculations for *R. diluvianum***

349 **Fig. S3** shows how the six steps outlined above and in **Fig. S2** are used to reconstruct absolute  
350 SST and  $\delta^{18}\text{O}_{\text{sw}}$  seasonality in *R. diluvianum*. Seasonality is clearer in  $\delta^{18}\text{O}_c$  than in  $\Delta_{47}$  (see **Fig.**  
351 **S3A**) due to the smaller relative error on individual  $\delta^{18}\text{O}_c$  analyses ( $2\sigma$  of 0.1‰ on a -2.0‰–0‰  
352 range) compared to  $\Delta_{47}$  analyses ( $2\sigma$  of 0.08‰ on a 0.62‰–0.73‰ range). The strong  $\delta^{18}\text{O}_c$   
353 seasonality lends confidence to the age model, resulting in a strong correlation between  
354 measured and modelled  $\delta^{18}\text{O}_c$  ( $R^2 = 0.72$ ;  $p < 0.001$ ; **Fig. S3B**). The model fit deteriorates in the  
355 last two growth years when growth slowed down, reducing the temporal sampling resolution.  
356 Sample size optimization (**Fig. S3C-D**) yielded two sample size windows ( $N = 22-25$  and  $N =$   
357  $50-53$ ) with optimal separation between the winter and summer sample (minima in p-curve; **Fig.**  
358 **2D**). This process was iterated in a Monte Carlo simulation ( $N = 1000$ ) yielding an average  
359 optimum sample size of 39.8 from which mean summer and winter SST and  $\delta^{18}\text{O}_{\text{sw}}$  and their  
360 uncertainties were reconstructed (**Fig S3E**). The resulting correlation between  $\delta^{18}\text{O}_c$  and  $\Delta_{47}$  ( $p$   
361  $\ll 0.05$ ) yields SST and  $\delta^{18}\text{O}_{\text{sw}}$  values for each aliquot which were grouped into monthly time  
362 bins (**Fig. S3F**; see also **Fig. 2** in main text). This procedure was repeated for *B. suecicus* and *A.*  
363 *incurva* (**Fig. 2** in main text).

364

### 365 **Climate model**

366 We chose to use the HadCM3L climate model because it is a highly developed coupled climate  
367 model and critically, to our knowledge the only one, to run Campanian specific boundary  
368 conditions with a range of  $p\text{CO}_2$  out to full equilibrium. Many other modelling communities are

369 unable to do this because of computer resource constraints and report findings based on un-  
370 equilibrated results. This is critical as we have shown that the deep ocean and hence ocean  
371 circulation can take at least 5000 modelled years to fully equilibrate to the applied boundary  
372 conditions, casting doubt on their validity. Our HadCM3L model has been improved from being  
373 highly utilized in IPCC intercomparison assessment reports. The model uses Campanian (78 Ma)  
374 continental configuration (after <sup>55</sup>Lunt et al., 2016; see **Fig. 1A**) and solar constant (~1356  
375 W\*m<sup>2</sup>), with a modern astronomical configuration and modern atmospheric conditions except  
376 for CO<sub>2</sub> concentrations (details in <sup>14</sup>Farnsworth et al., 2019). We evaluate model simulations  
377 with radiative forcing (*p*CO<sub>2</sub>) set to 560 ppmV (2× preindustrial concentration) and 1120 ppmV  
378 (4× preindustrial concentration), within the range of *p*CO<sub>2</sub> reconstructions for the Campanian as  
379 compiled by <sup>50</sup>. Global latitudinal gradients of summer, winter and MAT were exported from the  
380 top (10 m) ocean layer in the model output using zonal averages of all grid cells in longitudinal  
381 direction. Local SST seasonality was calculated as the average and variability of summer, winter  
382 and MAT in the 12 grid cells which mostly correspond to the paleolatitude of Kristianstad Basin  
383 (42.5-50°N, 7.5-15°E, see **Supplementary Data 5**). The model has a spatial resolution of 3.75°  
384 × 2.5° and uses 20 layers in ocean depth, of which the upper ocean box averages the top 10  
385 meters of the ocean. Hence the average SST of the Kristianstad Basin is biased against the  
386 shallowest coastal regions of the basin, such as the locality of *R. diluvianum*<sup>54,55</sup>. Our aim is not  
387 to compare the results of individual models and we do not claim that our model performs better  
388 than other models. In this study, the model is merely added to demonstrate how the new data can  
389 be used to verify model results. For comparison, modern SST data were obtained from the  
390 National Oceanic and Atmospheric Administration (<sup>28</sup>NOAA, 2020; see **Supplementary Data**  
391 **6**).

392

393 **REFERENCES**

- 394 56. Surlyk, F. & Christensen, W. K. Epifaunal zonation on an Upper Cretaceous rocky coast.  
395 *Geology* **2**, 529–534 (1974).
- 396 57. Kurevija, T., Vulin, D. & Krapec, V. Influence of Undisturbed Ground Temperature and  
397 Geothermal Gradient on the Sizing of Borehole Heat Exchangers. World Renewable Energy  
398 Congress 2011 (2011) doi:10.3384/ecp110571360.
- 399 58. de Winter, N. J. & Claeys, P. Micro X-ray fluorescence ( $\mu$ XRF) line scanning on  
400 Cretaceous rudist bivalves: A new method for reproducible trace element profiles in bivalve  
401 calcite. *Sedimentology* **64**, 231–251 (2016).
- 402 59. de Winter, N. J., Sinnesael, M., Makarona, C., Vansteenberge, S. & Claeys, P. Trace  
403 element analyses of carbonates using portable and micro-X-ray fluorescence: performance  
404 and optimization of measurement parameters and strategies. *Journal of Analytical Atomic*  
405 *Spectrometry* **32**, 1211–1223 (2017).
- 406 60. Vansteenberge, S. *et al.* Benchtop  $\mu$ XRF as a tool for speleothem trace elemental  
407 analysis: Validation, limitations and application on an Eemian to early Weichselian (125–  
408 97 ka) stalagmite from Belgium. *Palaeogeography, Palaeoclimatology, Palaeoecology* **538**,  
409 109460 (2020).
- 410 61. Al-Aasm, I. S. & Veizer, J. Diagenetic stabilization of aragonite and low-Mg calcite, I.  
411 Trace elements in rudists. *Journal of Sedimentary Research* **56**, 138–152 (1986).
- 412 62. Ivany, L. C. Reconstructing paleoseasonality from accretionary skeletal carbonates—  
413 challenges and opportunities. *The Paleontological Society Papers* **18**, 133–166 (2012).

- 414 63. Jones, D. S. Sclerochronology: reading the record of the molluscan shell: annual growth  
415 increments in the shells of bivalve molluscs record marine climatic changes and reveal  
416 surprising longevity. *American Scientist* **71**, 384–391 (1983).
- 417 64. Goodwin, D. H., Flessa, K. W., Schöne, B. R. & Dettman, D. L. Cross-calibration of  
418 daily growth increments, stable isotope variation, and temperature in the Gulf of California  
419 bivalve mollusk *Chione cortezi*: implications for paleoenvironmental analysis. *Palaios* **16**,  
420 387–398 (2001).
- 421 65. Schöne, B. R. *et al.* Climate records from a bivalved Methuselah (*Arctica islandica*,  
422 Mollusca; Iceland). *Palaeogeography, Palaeoclimatology, Palaeoecology* **228**, 130–148  
423 (2005).
- 424 66. Batenburg, S. J. *et al.* Interannual climate variability in the Miocene: High resolution  
425 trace element and stable isotope ratios in giant clams. *Palaeogeography, Palaeoclimatology,*  
426 *Palaeoecology* **306**, 75–81 (2011).
- 427 67. Steuber, T. Stable isotope sclerochronology of rudist bivalves: Growth rates and Late  
428 Cretaceous seasonality. *Geology* **24**, 315 (1996).
- 429 68. Surge, D., Lohmann, K. C. & Dettman, D. L. Controls on isotopic chemistry of the  
430 American oyster, *Crassostrea virginica*: implications for growth patterns. *Palaeogeography,*  
431 *Palaeoclimatology, Palaeoecology* **172**, 283–296 (2001).
- 432 69. Elliot, M. *et al.* Profiles of trace elements and stable isotopes derived from giant long-  
433 lived *Tridacna gigas* bivalves: potential applications in paleoclimate studies.  
434 *Palaeogeography, Palaeoclimatology, Palaeoecology* **280**, 132–142 (2009).

- 435 70. Steuber, T. Isotopic and chemical intra-shell variations in low-Mg calcite of rudist  
436 bivalves (Mollusca-Hippuritacea): disequilibrium fractionations and late Cretaceous  
437 seasonality. *International Journal of Earth Sciences* **88**, 551–570 (1999).
- 438 71. Freitas, P. S., Clarke, L. J., Kennedy, H., Richardson, C. A. & Abrantes, F.  
439 Environmental and biological controls on elemental (Mg/Ca, Sr/Ca and Mn/Ca) ratios in  
440 shells of the king scallop *Pecten maximus*. *Geochimica et Cosmochimica Acta* **70**, 5119–  
441 5133 (2006).
- 442 72. Surge, D. & Lohmann, K. C. Evaluating Mg/Ca ratios as a temperature proxy in the  
443 estuarine oyster, *Crassostrea virginica*. *Journal of Geophysical Research: Biogeosciences*  
444 **113**, (2008).
- 445 73. Ullmann, C. V., Böhm, F., Rickaby, R. E., Wiechert, U. & Korte, C. The Giant Pacific  
446 Oyster (*Crassostrea gigas*) as a modern analog for fossil ostreoids: isotopic (Ca, O, C) and  
447 elemental (Mg/Ca, Sr/Ca, Mn/Ca) proxies. *Geochemistry, Geophysics, Geosystems* **14**, 4109–  
448 4120 (2013).
- 449 74. Mouchi, V., de Rafélis, M., Lartaud, F., Fialin, M. & Verrecchia, E. Chemical labelling  
450 of oyster shells used for time-calibrated high-resolution Mg/Ca ratios: A tool for estimation  
451 of past seasonal temperature variations. *Palaeogeography, Palaeoclimatology,*  
452 *Palaeoecology* **373**, 66–74 (2013).
- 453 75. Mitchell, J. M. An overview of climatic variability and its causal mechanisms.  
454 *Quaternary Research* **6**, 481–493 (1976).
- 455 76. Huybers, P. & Curry, W. Links between annual, Milankovitch and continuum  
456 temperature variability. *Nature* **441**, 329 (2006).

- 457 77. Butler, P. G., Wanamaker, A. D., Scourse, J. D., Richardson, C. A. & Reynolds, D. J.  
458 Variability of marine climate on the North Icelandic Shelf in a 1357-year proxy archive  
459 based on growth increments in the bivalve *Arctica islandica*. *Palaeogeography,*  
460 *Palaeoclimatology, Palaeoecology* **373**, 141–151 (2013).
- 461 78. Marali, S. *et al.* Reproducibility of trace element time-series (Na/Ca, Mg/Ca, Mn/Ca,  
462 Sr/Ca, and Ba/Ca) within and between specimens of the bivalve *Arctica islandica* – A LA-  
463 ICP-MS line scan study. *Palaeogeography, Palaeoclimatology, Palaeoecology* **484**, 109–128  
464 (2017).
- 465 79. Kirby, M. X., Soniat, T. M. & Spero, H. J. Stable isotope sclerochronology of  
466 Pleistocene and Recent oyster shells (*Crassostrea virginica*). *Palaios* **13**, 560–569 (1998).
- 467 80. Buick, D. P. & Ivany, L. C. 100 years in the dark: Extreme longevity of Eocene bivalves  
468 from Antarctica. *Geology* **32**, 921–924 (2004).
- 469 81. Dauphin, Y., Cuif, J. P., Mutvei, H. & Denis, A. Mineralogy, chemistry and  
470 ultrastructure of the external shell-layer in ten species of *Haliotis* with reference to *Haliotis*  
471 *tuberculata* (Mollusca: Archaeogastropoda). *Bulletin of the Geological Institutions of the*  
472 *University of Uppsala* **15**, 7–37 (1989).
- 473 82. Schöne, B. R., Dunca, E., Fiebig, J. & Pfeiffer, M. Mutvei's solution: An ideal agent for  
474 resolving microgrowth structures of biogenic carbonates. *Palaeogeography,*  
475 *Palaeoclimatology, Palaeoecology* **228**, 149–166 (2005).
- 476 83. Barbin, V., Ramseyer, K. & Elfman, M. Biological record of added manganese in  
477 seawater: a new efficient tool to mark in vivo growth lines in the oyster species *Crassostrea*  
478 *gigas*. *International journal of earth sciences* **97**, 193–199 (2008).

- 479 84. Ballesta-Artero, I. *et al.* Environmental and biological factors influencing trace  
480 elemental and microstructural properties of *Arctica islandica* shells. *Science of the Total*  
481 *Environment* **645**, 913–923 (2018).
- 482 85. Goodwin, D. H., Schöne, B. R. & Dettman, D. L. Resolution and fidelity of oxygen  
483 isotopes as paleotemperature proxies in bivalve mollusk shells: models and observations.  
484 *Palaios* **18**, 110–125 (2003).
- 485 86. Durham, S. R., Gillikin, D. P., Goodwin, D. H. & Dietl, G. P. Rapid determination of  
486 oyster lifespans and growth rates using LA-ICP-MS line scans of shell Mg/Ca ratios.  
487 *Palaeogeography, Palaeoclimatology, Palaeoecology* **485**, 201–209 (2017).
- 488 87. de Winter, N. J. *et al.* Subdaily-Scale Chemical Variability in a *Torreites Sanchezi*  
489 Rudist Shell: Implications for Rudist Paleobiology and the Cretaceous Day-Night Cycle.  
490 *Paleoceanography and Paleoclimatology* **35**, e2019PA003723 (2020).
- 491 88. Wilkinson, B. H. & Ivany, L. C. Paleoclimatic inference from stable isotope profiles of  
492 accretionary biogenic hardparts – a quantitative approach to the evaluation of incomplete  
493 data. *Palaeogeography, Palaeoclimatology, Palaeoecology* **185**, 95–114 (2002).
- 494 89. Goodwin, D. H., Paul, P. & Wissink, C. L. MoGroFunGen: A numerical model for  
495 reconstructing intra-annual growth rates of bivalve molluscs. *Palaeogeography,*  
496 *Palaeoclimatology, Palaeoecology* **276**, 47–55 (2009).
- 497 90. Lough, J. M. & Barnes, D. J. Environmental controls on growth of the massive coral  
498 *Porites*. *Journal of Experimental Marine Biology and Ecology* **245**, 225–243 (2000).
- 499 91. Adey, W. H. & Vassar, J. M. Colonization, succession and growth rates of tropical  
500 crustose coralline algae (Rhodophyta, Cryptonemiales). *Phycologia* **14**, 55–69 (1975).

- 501 92. Gentry, D. K. *et al.* Stable Isotope and Sr/Ca Profiles From the Marine Gastropod *Conus*  
502 *ermineus*: Testing a Multiproxy Approach For Inferring Paleotemperature and Paleosalinity.  
503 *PALAIOS* **23**, 195–209 (2008).
- 504 93. Rodríguez-Sanz, L. *et al.* Penultimate deglacial warming across the Mediterranean Sea  
505 revealed by clumped isotopes in foraminifera. *Scientific Reports* **7**, 1–11 (2017).
- 506